DTU Library

A model for modifying the S-N curve considering the effect of boundary conditions on the fatigue crack growth of welded components

Shakeri, Iman; Wu, Weijian; Michel, Alexander; Eder, Martin A.

ORIGINAL ARTICLE

FFEMS Fatigue & Fracture of Engineering Materials & Structures **WILEY**

A model for modifying the S-N curve considering the effect of boundary conditions on the fatigue crack growth of welded components

Iman Shakeri[1,2] | Weijian Wu[3] | Alexander Michel[4] | Martin A. Eder[2]

[1]Faculty of Civil Engineering and Geosciences, Department of Engineering Structures, Delft University of Technology, Delft, Netherlands

[2]Department of Wind and Energy Systems, Technical University of Denmark, Roskilde, Denmark

[3]Department of Civil and Mechanical Engineering, Technical University of Denmark, Lyngby, Denmark

[4]Department of Environmental and Resource Engineering, Technical University of Denmark, Lyngby, Denmark

Correspondence
Iman Shakeri, Faculty of Civil Engineering and Geosciences, Department of Engineering Structures, Delft University of Technology, Netherlands.
Email: I.Shakeri-1@tudelft.nl; iman.shakeri1368@gmail.com

Funding information
Danish Offshore Technology Centre

Abstract
The present study proposes a novel model to modify master S-N curves of components according to their load redistribution capability reflected in different boundary conditions (BCs) based on the fracture mechanics analysis. To that end, a comprehensive numerical study was conducted on a Single Edge Notch Bend (SENB) specimen constrained with different kinematic BCs using discrete fatigue crack growth (FCG) simulation. It was observed that BCs indeed can have a significant effect on the crack growth behavior and consequently on the resulting fatigue life under the same nominal loading conditions. The proposed model was applied to the S-N curve of a T-welded joint, and the predicted fatigue life was validated against 3D FCG simulations. Finally, FCG tests were conducted on SENB specimens to experimentally corroborate the effect of BCs on the FCG rate.

KEYWORDS
boundary conditions, fatigue crack growth, fatigue design, fatigue life, S-N curve, welded joints

Highlights

- Boundary conditions significantly affect crack growth, fatigue life, and S-N curve.
- Increase accuracy of S-N curve predictions by considering boundary condition effects.
- Proposed model is straight forward to apply through application of a restraint factor.
- Application of model is shown using fatigue crack growth simulation of T-welded joint.

—WILEY

1 | INTRODUCTION

High cycle fatigue is widely recognized by the industry as well as the research community as an important element in the design, maintenance, and repair of structures in general, with a particular emphasis on offshore structures.[1]

Structures are ideally designed to ensure economical operation throughout the design service life in compliance with given requirements and acceptance criteria. Standards and design codes[2–4] currently in effect describe a safe life methodology in which the fatigue strength is based on a material stress-life (S-N) diagram that relates the number of cycles (N) to failure with the applied stress range (nominal or hot-spot) of the intact geometry.

Deterioration processes such as fatigue and crack growth will always be present to some degree, and depending on the adapted design philosophy (in terms of degradation allowance and protective measures), deterioration processes may reduce performance beyond what is acceptable. In order to ensure that the given acceptance criteria are fulfilled throughout the service life, it may thus be necessary to control the development of deterioration. In typical practical applications, inspection is the most relevant and effective means of deterioration control. Such an approach has the advantage that any fatigue or fracture that occurs has a finite chance of being detected before severe consequences—such as catastrophic failure—can develop. Over the past decades, a large number of offshore structures (e.g., offshore wind turbines, pipelines, and platforms) have been designed and installed in aggressive and harsh marine environments. Operating such assets entails significant maintenance costs that are spent annually, including vessel transport and logistics and diving operations for underwater inspection campaigns. Thus, more accurate fatigue life prediction capabilities are vital for reducing operation and maintenance (O&M) costs by optimal design and for more economically predictive inspection planning. Furthermore, particularly in offshore structures, a weight reduction obtained by an optimized design can lead to the achievement of considerable savings in support substructures.[5]

Sometimes mechanical components designed to withstand cyclic loading are found to be subjected to service conditions that have not been taken into account at the design stage. For example, backlash modification between the parts due to wear and severe operating conditions might also contribute to a change in the internal boundary conditions (BCs), leading to unexpected loads acting on the component. In this sense, an unexpected BC may affect the crack propagation life.[6] Suppose the dimensioning of the component is based on the damage tolerance design philosophy. In that case, these influence both the inspection strategies and the inspection methods and intervals, which must guarantee the prevention of catastrophic failure due to fatigue experienced during its service life.[7]

To the best knowledge of the authors, current standards and design codes (e.g., Eurocode 3, Part 9[2], IIW,[3] and DNV[4]) neglect the effect of BCs on the fatigue life of components (e.g., welded joints) with otherwise identical geometries and loading as schematically depicted in Figure 1. It is seen that, for example, Eurocode 3 Part 9 predicts equal fatigue life for the same detail category and nominal loading in the intact geometry irrespective of the BCs, while observations available in the open literature strongly indicate that BCs may indeed affect the fatigue crack growth (FCG).[6,8,9] Therefore, it can be inferred that using the S-N approach currently stipulated in prominent design codes can lead to an overly conservative fatigue life prediction and hence lead to uneconomical O&M. It should be noted that the situation presented in Figure 1 also applies to the hot-spot method, in which case the load is scaled such that the three hot-spot stresses are identical. It can be expected that compared to case (A), cases (B) and (C) can activate additional load-carrying capacity during FCG that ultimately reflects in increased fatigue lifetime—hardly supported by a single S-N curve.

As later demonstrated in the present study, the investigated effect of BCs has little to negligible influence on the initiation life. However, the influence of the BCs increases as the crack grows. It must be emphasized that it is not the intention of the authors to criticize current design standards and best practices as they are conservative and safe but rather to point out that the consideration of BC effects may become important if a more accurate lifetime prediction is of concern, for example, for lifetime extension purposes.

The accuracy of the fatigue damage hypothesis is closely linked to how the design S-N curve is established. Several studies[10–12] have investigated the effect of various parameters on the initiation of fatigue cracks; however, if more accurate fatigue lifetime predictions are of concern (e.g., for economic inspection planning and O&M cost reduction), the influence of BCs on the fatigue crack propagation behavior should not be neglected. Numerous studies[13–20] have explored fatigue crack propagation under various loading conditions. For instance, Barsoum Z. and Barsoum I.[14] and Božić et al.[15,16] have examined the effect of welding residual stress on fatigue crack propagation through finite element (FE) analysis. Tang et al.[17] and Ince[18] have investigated the influence of high-frequency mechanical impact treatment on fatigue crack propagation in welded joints, employing the weight
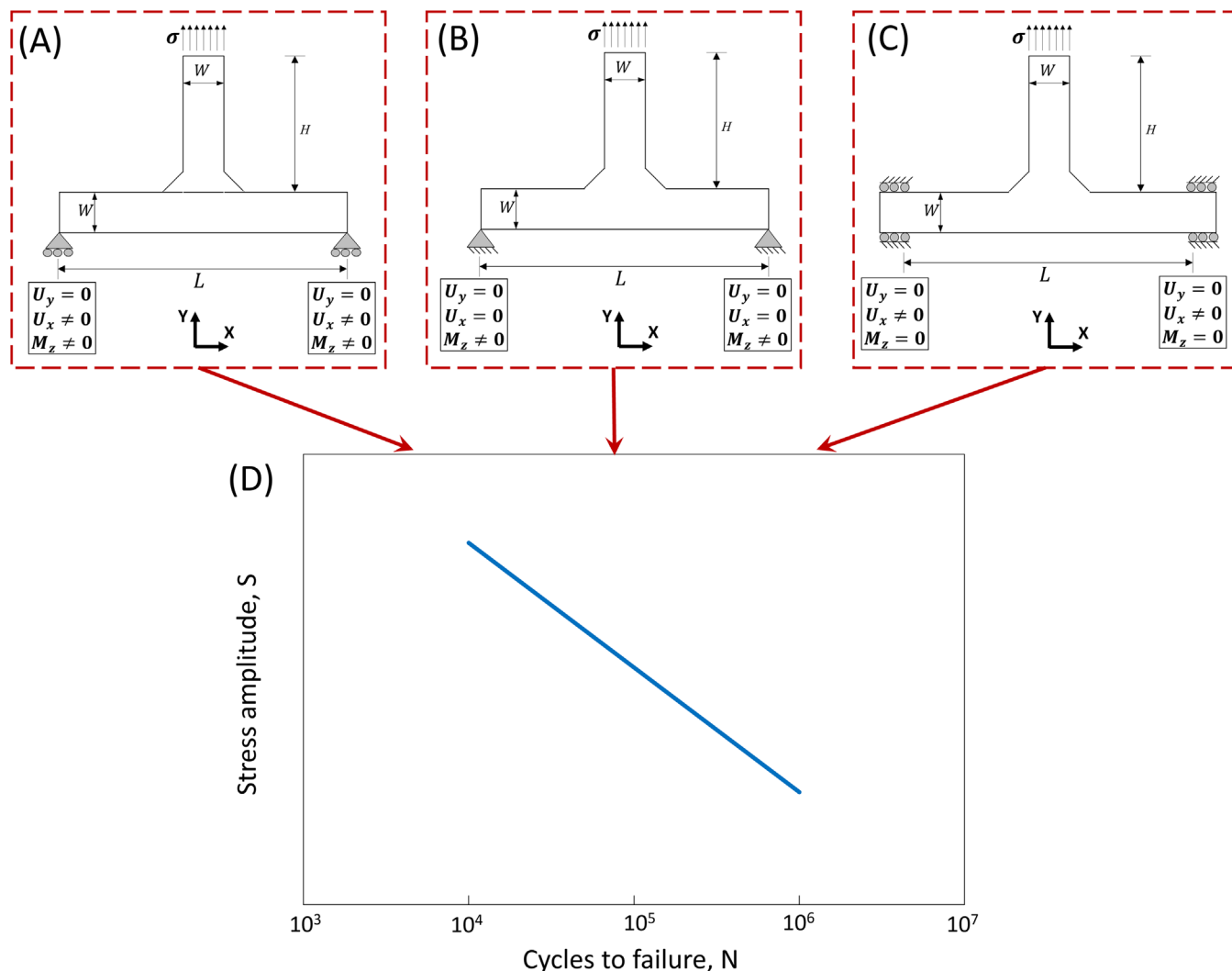
FIGURE 1 Schematic representation of equal fatigue life prediction based on a single "master" S-N curve stipulated in current design codes exemplary for a typical T-welded joint restrained by three different BCs but with otherwise identical geometry and nominal loading for (A) simply supported, (B) doubly pinned, and (C) rotationally fixed constraints. [Colour figure can be viewed at wileyonlinelibrary.com]

function method for calculating stress intensity factor (SIF). However, literature investigating the effect of BCs on the high cycle fatigue life is scarce.

Petinov et al.[21] mentioned that S-N diagrams based on the test results are incomplete and may need to be adjusted, and they claimed that the initial phase of the fatigue life and the subsequent crack propagation should be analyzed separately by considering the effects of the surrounding structure and loading. Therefore, they devised an experiment in their work with the aim of investigating the FCG in T-welded joints under consideration of the influence of component shape and BC during fatigue testing. They concluded that the effects of the surrounding structure should be taken into account during FCG, but a specific calculation method was not provided.

Shahani and Shakeri[22] analytically studied the effect of BCs on the stress and displacement distributions at the

vicinity of the crack tip in a functionally graded material and showed that the order of stress singularity depends on the BCs. In addition, it was shown elsewhere[23] that crack growth may change the initial stress distribution in front of the crack and thus affect the fatigue life. Employing photo-elastic measurement techniques, Singh et al.[24] have shown that BCs may also affect the SIF of the inclined crack.

Sun et al.[8] performed a fatigue experiment on a T-welded joint by clamping the specimen on both ends of the beam (i.e., fully fixed BCs). They found that the crack growth behavior in their experiment is different compared to their previous observations on simply supported conditions. Their experimental results corroborate the fact that fatigue life can be significantly affected by the surrounding BCs. Sun et al. proposed a modification of the Paris' equation to predict crack growth in their experiments.

Pucillo et al.[6,9] have numerically investigated the effect of additional unilateral BC on the SIF for a crack existing at a shoulder fillet notch in a circular stepped bar under bending using the Virtual Crack Closure Technique. They considered a unilateral BC to simulate the interaction of the shaft with a generic body. Their results show that the presence of a unilateral BC at the shoulder fillet notch significantly affects the SIF; however, the shape of the crack front does not change during growth. Also, it has been stated that the occurrence of contact at the shoulder of the shaft has a beneficial effect on the crack propagation life.

Based on the reviewed literature, it is found that the effect of BCs is not yet well understood and not properly considered in the current standards and design codes, and there is a lack of a suitable model to predict the fatigue life considering various BCs.

The present study aims to investigate the effect of BCs on the fatigue crack propagation behavior and fatigue life of a metallic structure. To this end, a comprehensive numerical study is first performed on a single edge notch bend (SENB) specimen subjected to various BCs by employing numerical fracture mechanics analysis. It is shown that BCs have a significant and vastly different influence on crack growth and fatigue life, which ultimately affects the associated S-N curves. Thereafter, the proposed model is applied to a T-welded joint and validated against a three-dimensional FCG simulation. At the end, constant amplitude FCG experiments are performed on SENB specimens to demonstrate and corroborate the numerically predicted effect of BCs on the fatigue crack growth rate (FCGR) in statically indeterminate components.

Novelty: The novel model proposed modifies the master S-N curve using a restraint factor to more accurately consider the effect of different BCs on fatigue life.

Significance: The proposed model increases the fidelity of S-N-based fatigue lifetime predictions of structural components that the authors deem particularly useful for more economical inspection planning of offshore structures to reduce O&M costs. The proposed approach is fully compatible with existing S-N-based approaches in the design standards, and its implementation is straightforward.

2 | MODELS AND METHODS

2.1 | The considered geometry and BCs

The SENB specimen, as illustrated in Figure 2A, was chosen for the investigation. This specimen is geometrically
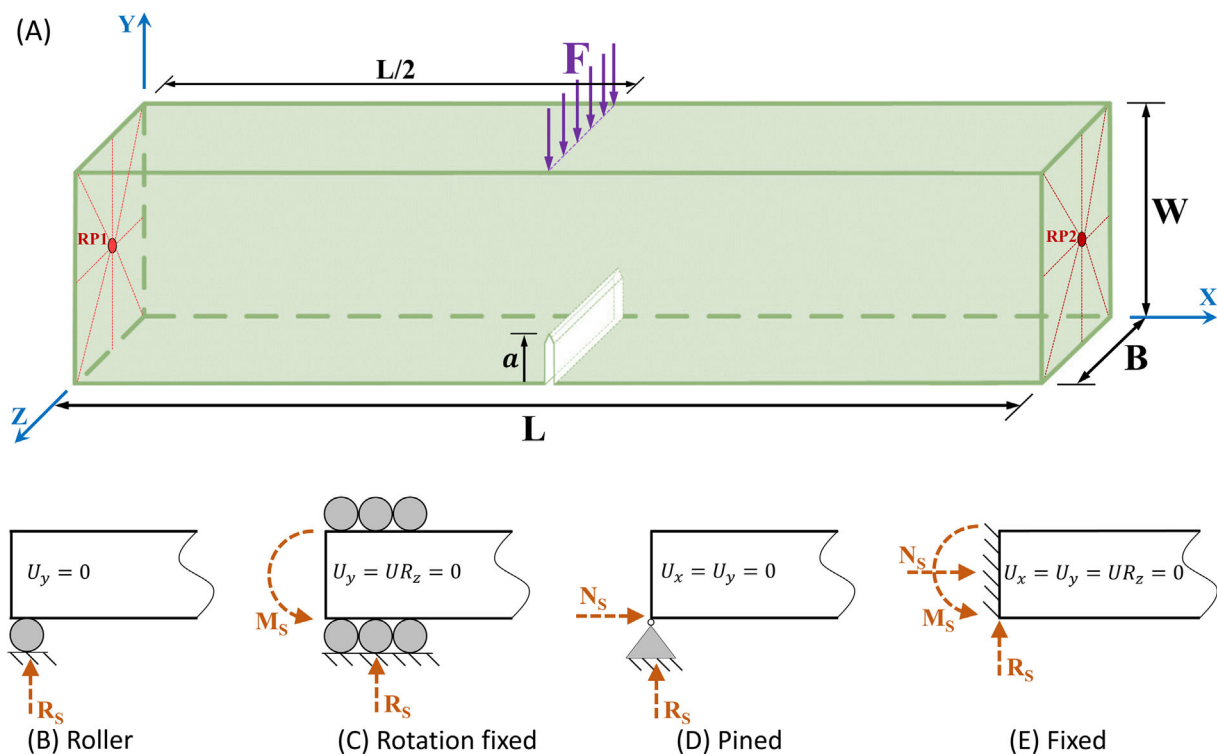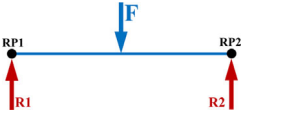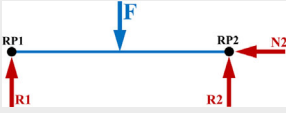
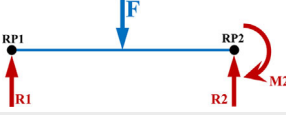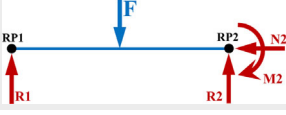**FIGURE 2** (A) Geometry of the SENB specimen shown in a three-point bending setup. Four different types of BCs considered in this investigation (B) roller ("*Rol*") and (C) rotation ("*Rot*") and (D) pinned ("*Pin*") and (E) fixed ("*Fix*"). [Colour figure can be viewed at wileyonlinelibrary.com]

similar to a butt-welded joint, neglecting details of the weld bead. This simplification was made to conduct a more efficient normalized study and gain a better understanding of the effect of BCs. However, it should be noted that the proposed approach is not limited to this specific geometry.

The material considered is structural steel, which is modeled using an isotropic linear elastic material model with Young's modulus of E = 210 GPa and Poisson's ratio of $\nu = 0.3$.

A concentrated force was applied at mid-span as a line-load where different BCs could be applied to the reference points (RPs) indicated as red dots rigidly coupled to the respective beam end faces. For a plane problem, four types of BCs can be considered for each support as illustrated in Figure 2: (B) roller support restricting the displacement in the Y direction, (C) rotation fixed support restricting the rotation in the Z direction, (D) pin support restricting the displacement in X and Y directions, and (E) a fully fixed support
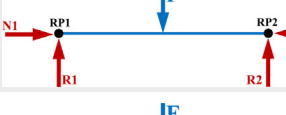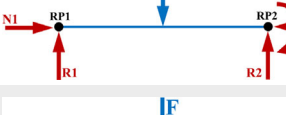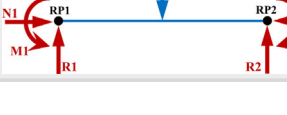
TABLE 1 Combinations of various support conditions and their corresponding BCs with the nominal mid-span bending stress at the top and bottom surfaces of the intact geometry.

Name	Force and moment reactions at supports	BCs at RP		$M_{L/2}$	$S^{nom}_{max@L/2}$
		RP1	RP2		
Rol-Rol		$U_x \neq 0$, $U_y = 0$, $UR_z \neq 0$	$U_x \neq 0$, $U_y = 0$, $UR_z \neq 0$	$\frac{1}{4}FL$	$\frac{3}{2}\frac{FL}{BW^2}$
Rol-Pin		$U_x \neq 0$, $U_y = 0$, $UR_z \neq 0$	$U_x = 0$, $U_y = 0$, $UR_z \neq 0$	$\frac{1}{4}FL$	$\frac{3}{2}\frac{FL}{BW^2}$
Rol-Rot		$U_x \neq 0$, $U_y = 0$, $UR_z \neq 0$	$U_x \neq 0$, $U_y = 0$, $UR_z = 0$	$\frac{5}{32}FL$	$\frac{15}{16}\frac{FL}{BW^2}$
Rol-Fix		$U_x \neq 0$, $U_y = 0$, $UR_z \neq 0$	$U_x = 0$, $U_y = 0$, $UR_z = 0$	$\frac{5}{32}FL$	$\frac{15}{16}\frac{FL}{BW^2}$
Rot-Pin		$U_x \neq 0$, $U_y = 0$, $UR_z = 0$	$U_x = 0$, $U_y = 0$, $UR_z \neq 0$	$\frac{5}{32}FL$	$\frac{15}{16}\frac{FL}{BW^2}$
Rot-Rot		$U_x \neq 0$, $U_y = 0$, $UR_z = 0$	$U_x \neq 0$, $U_y = 0$, $UR_z = 0$	$\frac{1}{8}FL$	$\frac{3}{4}\frac{FL}{BW^2}$
Rot-Fix		$U_x \neq 0$, $U_y = 0$, $UR_z = 0$	$U_x = 0$, $U_y = 0$, $UR_z = 0$	$\frac{1}{8}FL$	$\frac{3}{4}\frac{FL}{BW^2}$
Pin-Pin		$U_x = 0$, $U_y = 0$, $UR_z \neq 0$	$U_x = 0$, $U_y = 0$, $UR_z \neq 0$	$\frac{1}{4}FL$	$\frac{3}{2}\frac{FL}{BW^2}$
Pin-Fix		$U_x = 0$, $U_y = 0$, $UR_z \neq 0$	$U_x = 0$, $U_y = 0$, $UR_z = 0$	$\frac{5}{32}FL$	$\frac{15}{16}\frac{FL}{BW^2}$
Fix-Fix		$U_x = 0$, $U_y = 0$, $UR_z = 0$	$U_x = 0$, $U_y = 0$, $UR_z = 0$	$\frac{1}{8}FL$	$\frac{3}{4}\frac{FL}{BW^2}$

restricting rotation in the Z direction and the displacement in X and Y directions. The rotation fixed BC can be achieved by a row of rollers located on both the top and bottom sides of the specimen. Vertical reaction force (R_S), horizontal reaction force (N_S), and reaction moment (M_S) carried by each support are schematically shown in Figure 2B–E.

All possible combinations of the aforementioned BCs shown in Figure 2B–E are listed in Table 1. The resulting bending moment distributions and bending moments at mid-span were determined analytically using the first-order Euler–Bernoulli beam theory. In the SENB, the bending stress component in the X direction (perpendicular to the crack plane) governs the crack growth. For the SENB geometry without a crack (i.e., the intact geometry), the maximum value of the nominal stress in the X direction at mid-span was calculated using the well-known Navier equation as follows:

$$S_{xx,\text{max}}^{\text{nom}} = \frac{M_{L/2}W}{2I} \quad (1)$$

where $M_{L/2}$ is the bending moment at $x = L/2$ and $I = BW^3/12$ is the second moment of area about the Z axis. The values of $S_{xx,\text{max}}^{\text{nom}}$ for each case are also provided in Table 1 for the center load.

It can be seen from Table 1 that the nominal stress is identical for some cases. Therefore, using the nominal stress approach to predict the fatigue life based on a single "master" S-N curve leads to the same results for the following cases:

- Rol-Rol = Rol-Pin = Pin-Pin
- Rol-Rot = Rol-Fix = Rot-Pin = Pin-Fix
- Rot-Rot = Rot-Fix = Fix-Fix

On the other hand, it is evident that cases with identical nominal stresses do not necessarily render the same fatigue life. This emphasizes the inadequacy of the nominal stress to predict the fatigue life when used as the only metric due to negligence of the BC-dependent stress redistribution capabilities caused by crack growth.

2.2 | The FE model

Among the various methods for calculating the SIF, FE and the weight function methods are commonly used. The weight function method is computationally efficient and considers the effect of residual stress.[17,18] However, its precision can be sometimes problematic in cases of non-planar crack growth, and it does not account for the redistribution of residual stresses due to crack growth. In the present study, the FE method was utilized and is described in the following.

Three-dimensional simulation of the FCG was performed using the commercial FE software package Abaqus[25] and Zencrack.[26] The maximum energy release rate is used as the criterion for predicting the crack growth direction. Then, the energy release rate is calculated in each node on the crack front, and the maximum value of the energy release rate and its growth direction are extracted, and thereafter, the amount of growth is determined, and the crack front is updated.[27] Due to potential variations in the growth increment among different nodes on the crack front, a curved crack front with a thumbnail shape may ensue.[23]

To apply the BCs to the specimen, as shown in Figure 2A, RPs are placed at the center of surfaces on both sides of the beam. Each RP is coupled to its corresponding surface using a kinematic (rigid) coupling constraint (Figure 2A).

The assumptions of linear elastic fracture mechanics are used for the FE analysis of FCG, and the material behavior is assumed to be linear elastic. Hexagonal quadratic (20 node) solid elements with reduced integration (Abaqus type C3D20R) were employed for the 3D FE model. Wedge elements with a square root singular shape function and size of 0.125 mm were assigned to the crack front in the typical "spider-web" array. Finally, the model was discretised using 6656 elements and 30,960 nodes.

An initial through crack $a_i/W = 0.033$ was introduced in the middle of the SENB specimen. Simulations were conducted for $L/W = 3.33, 5, 6.67, 10, 13.33$ (in all cases $B/W = 0.5$ and $W = 15$ mm) by using a Python[28] script allowing for convenient parameterization. Values of SIFs were obtained from the J-integral using the interaction integral method[25] as follows:

$$K_{\text{I}} = \frac{E}{2(1-\lambda\nu^2)}J_{\text{int}}^{\text{I}}$$
$$K_{\text{II}} = \frac{E}{2(1-\lambda\nu^2)}J_{\text{int}}^{\text{II}} \quad (2)$$
$$K_{\text{III}} = \frac{E}{2(1+\nu)}J_{\text{int}}^{\text{III}}$$

where J_{int} is interaction integral, $\lambda = 0$ for plane stress, and $\lambda = 1$ for plane strain. Some cases in Table 1 (e.g., Rol-Fix) are not symmetric; therefore, the value of the mode II SIF (K_{II}) is not zero at the initial stages of crack growth. However, the maximum value of $K_{\text{II}}/K_{\text{I}}$ is 0.003, which shows that mode I is dominant in all cases, and consequently, the mode I SIF (K_{I}) was used for the fatigue life calculation. As the values of K_{II} are significantly lower than K_{I}, the coupled modes' effect[29] is deemed negligible in this study.

2.3 | FCG prediction

A cyclic load ratio of $R = F_{min}/F_{max} = 0$ was adopted. The Paris–Erdogan equation is employed to calculate the fatigue life:

$$\frac{da}{dN} = g(a) = C_p(\Delta K_{\mathrm{I}})^{n_p} \qquad (3)$$

where $C_p = 1.5 \times 10^{-30}$ (based on units in Pa and m) and $n_p = 3.082$ are chosen representatives for structural steel S355.[30] In order to facilitate a comparison of the SIF results of various cases, a mode I geometric function is defined as follows:

$$Y_{\mathrm{I}} = \frac{K_{\mathrm{I}}}{S_{xx,\max}^{\mathrm{nom}}\sqrt{\pi a}} \qquad (4)$$

2.4 | S-N diagram

S-N curves of each representative case were predicted using Equations (3) and (5) by varying the cyclic load amplitudes. The applied load was chosen in such a way that the maximum nominal bending stress ($S_{xx,\max}^{\mathrm{nom}}$) was the same for all cases. The number of cycles to failure was computed by numerical integration of the growth rate (Equation 3) using the trapezoidal rule for uniform spacing as follows:

$$N_f = \int_{a_i}^{a_c} \frac{1}{g(a)}\mathrm{d}a \approx \frac{a_c - a_i}{2k} \sum_{j=i+1}^{k}\left(\frac{1}{g(a_{j-1})} + \frac{1}{g(a_j)}\right) \qquad (5)$$

where k is the number of terms in the series. The critical crack length (a_c) was obtained by satisfying the condition $K_{\mathrm{I,max}} = K_{\mathrm{IC}}$ upon which the analysis was stopped. The fracture toughness was assumed to be $K_{\mathrm{IC}} = 30\,\mathrm{MPa}\sqrt{\mathrm{m}}$.

S-N curves are described by a linear relationship (Equation 6) between the number of cycles to failure (N_f) and the range of applied nominal stress in the log–log plot scale.

$$N_f = A(\Delta S_{xx,\max}^{\mathrm{nom}})^{-m} \qquad (6)$$

where m and A are the inverse slope and constant of the S-N curve in the log–log plot. The value of m in Equation (6) can be obtained by the linear regression method. It is noteworthy to mention that for calculating m from linear regression, $\log N$ was plotted versus $\log \sigma$;

that is, the number of cycles to failure should be treated as a dependent variable.[31]

It should be noted that an experimental S-N curve includes the number of cycles to failure, encompassing both crack initiation and propagation life, whereas the number of cycles to failure predicted by Equation (5) only considers the crack propagation life. Welded joints often contain material defects induced by the welding process. Given that these defects act as initial cracks, the crack initiation period in welded joints is relatively short compared to the overall lifetime of the welded parts[18]. Therefore, employing the crack growth-based fatigue life prediction approach (i.e., Equation 5) is a reasonable method to predict the number of cycles to failure of the welded joints.

3 | RESULTS AND DISCUSSION

3.1 | Effect of BCs on the SIF

In order to validate the adopted 3D FE simulation method of FCG, the SIF results for the Rol-Rol case with $L/W = 10$ are compared with the values presented by Fett[32] as shown in Figure 3 (black diamonds). The SIF for the node located on the mid-thickness (B/2), which is closer to the plane strain conditions, was used for the verification purpose as well as fatigue life estimation (i.e., Equation 3). The maximum difference between the SIF predicted from the present study (red graph) and those presented in Fett[32] is 3%, which indicates that the
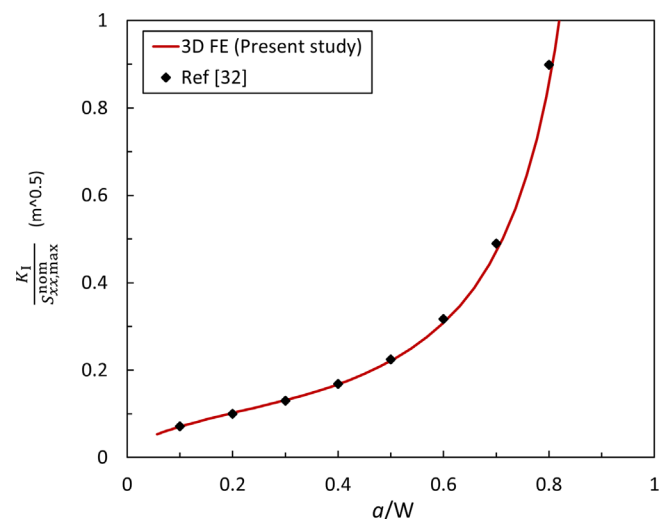

FIGURE 3 Comparison of K_{I} over nominal maximum bending stress versus normalized crack length obtained from the present model and Fett[32]. [Colour figure can be viewed at wileyonlinelibrary.com]
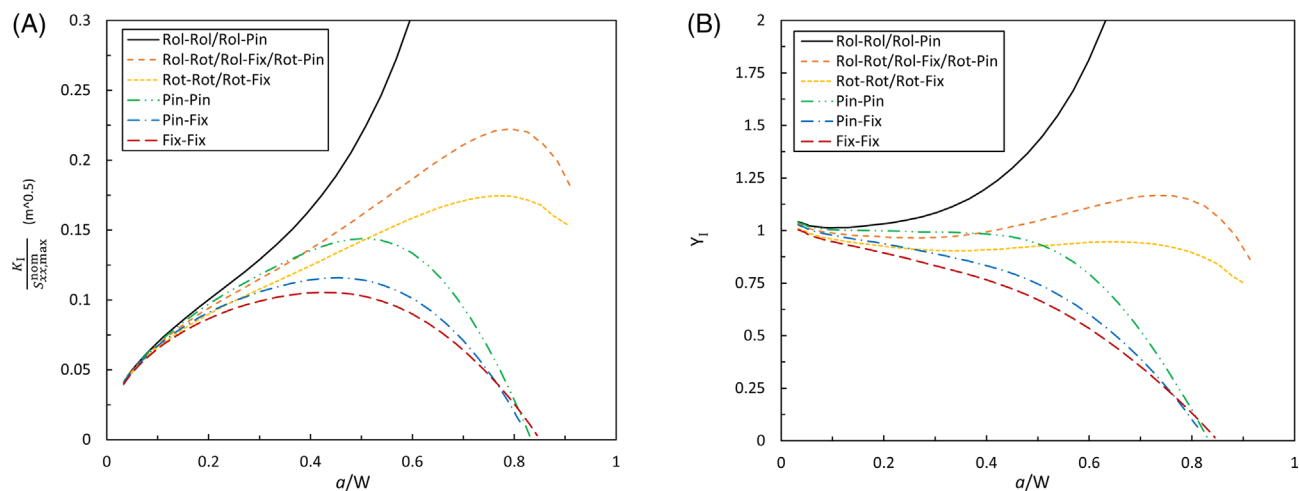
FIGURE 4 Variation of (A) the SIF and (B) geometric function Y_I, as a function of the normalized crack length for different BCs for the SENB geometry with $L/W = 6.67$ showing the decelerating effect of static indeterminacy on the crack growth where activation of membrane action exhibits the strongest influence. [Colour figure can be viewed at wileyonlinelibrary.com]

FIGURE 5 Variation of (A) SIF for Pin-Pin, (B) SIF for Fix-Fix, (C) Y_I for Pin-Pin, and (D) Y_I Fix-Fix, in terms of normalized crack length for different L/W ratios. [Colour figure can be viewed at wileyonlinelibrary.com]

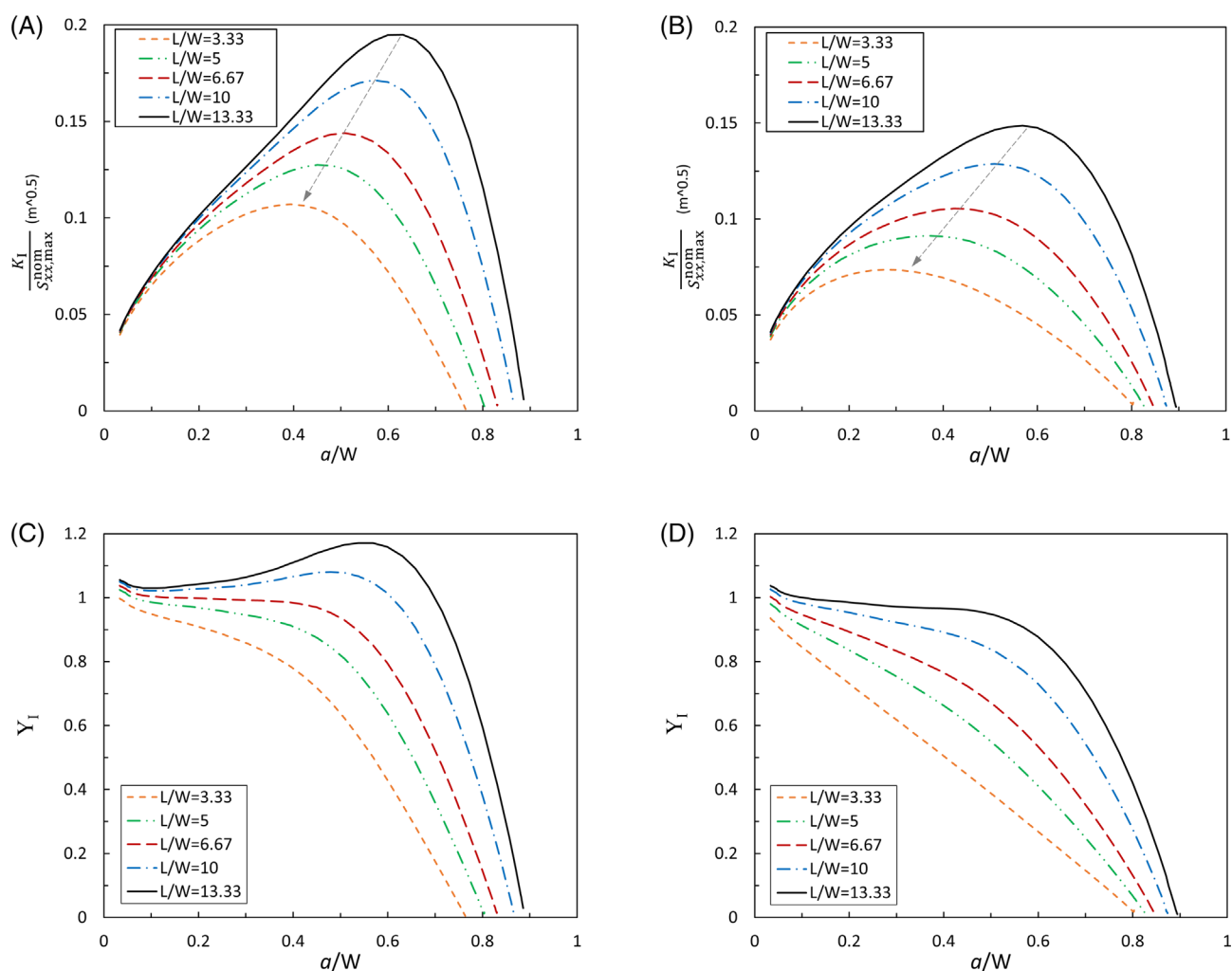3D FE model provides sufficiently accurate FCG predictions for the cases investigated in this work.

Figure 4A shows the effect of BCs on the SIF, and Figure 4B shows the geometric function (c.f. Equation 4) for the SENB geometry with $L/W = 6.67$. Numerical crack growth analysis revealed that the results of some BC cases listed in Table 1 are precisely the same, notably:

- Rol-Rol = Rol-Pin
- Rol-Fix = Rol-Rot = Rot-Pin
- Rot-Rot = Rot-Fix

This observation agrees with the expected behavior inasmuch as a single-sided restraint of the horizontal displacement does not enable any load redistribution effects during crack growth.

It can be seen in Figure 4 that the SIFs and, consequently, Y_I are asymptotic for all BCs for the initial growth phase, indicating that the SIF is largely independent of the BCs for cracks $a/W \leq 0.1$, while the BCs rapidly gain influence on the SIF and Y_I for $a/W > 0.2$. In general, it becomes evident that adding more restraints decreases the SIF since, in statically indeterminate systems, a greater amount of the applied load can be redistributed by the activation of redundant load-carrying capacity provided by the supports. Except for the case of Rol-Rol, where the SIF increases monotonically with increasing crack length, the SIF in the remaining cases decreases at a specific crack length and eventually leads to crack growth retardation. An interesting observation is that in cases where the horizontal displacement is restrained in both supports (i.e., $U|_{x=0} = U|_{x=L} = 0$), a
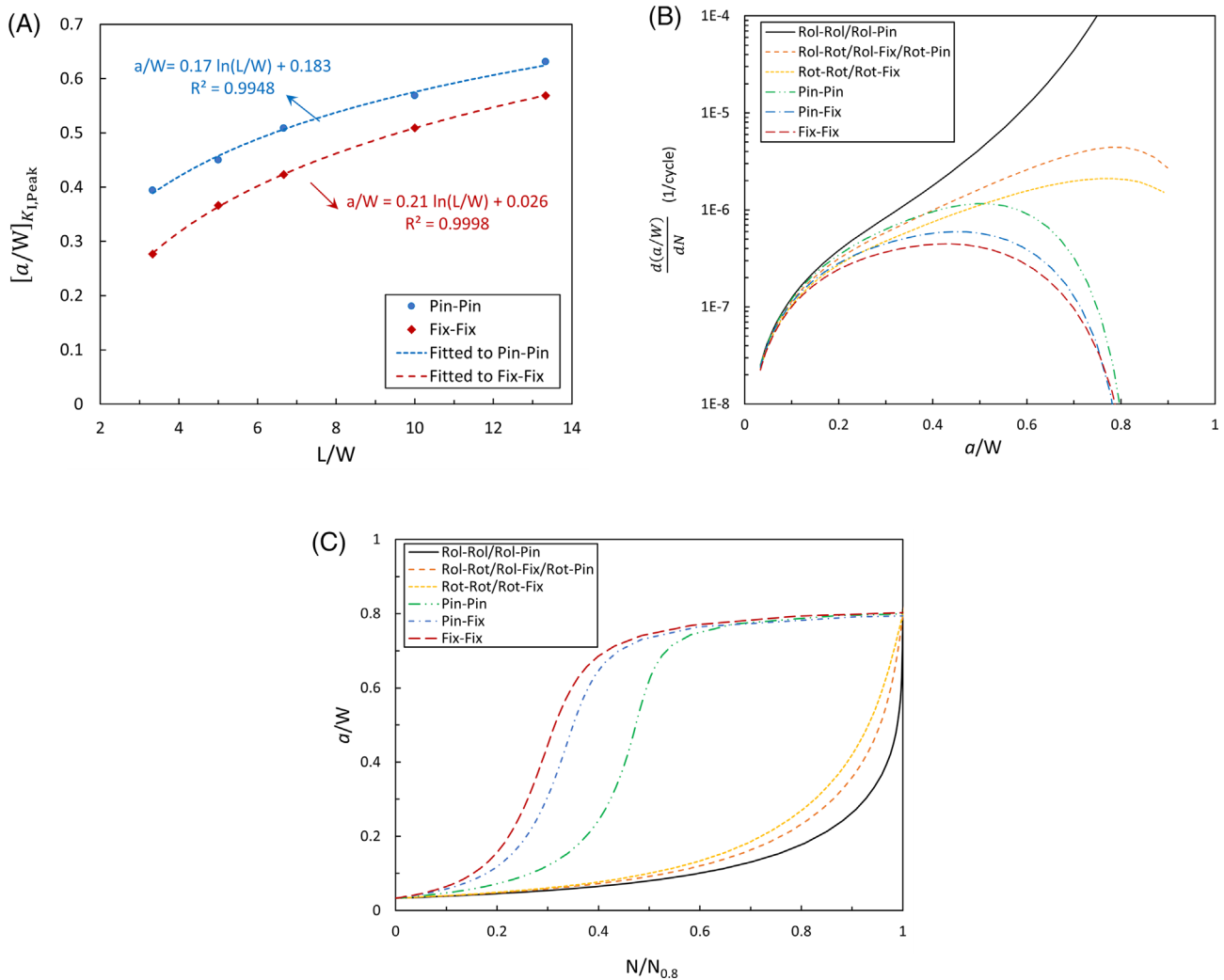
FIGURE 6 (A) Changes in crack length corresponding to the peak SIF ($[a/W]_{K_{I,Peak}}$) in terms of the normalized beam length (L/W) for the extreme BC cases Pin-Pin and Fix-Fix following a logarithmic function. (B) Effect of BCs on the FCGR for the SENB geometry with $L/W = 6.67$. (C) Normalized FCG histories for the SENB geometry with $L/W = 6.67$ subjected to various BCs. [Colour figure can be viewed at wileyonlinelibrary.com]

crack arrest occurs, that is, $K_I \to 0$, owing to activation of membrane action.

By comparing the results of the cases Pin-Pin and Rot-Rot in Figure 4A,B, it can be seen that for a crack $0.2 < a/W < 0.5$, restraining the rotation (Rot-Rot) has a more significant effect on controlling the crack growth, while for a larger crack ($a/W > 0.5$), restraining the horizontal displacement (Pin-Pin) plays a more significant role in controlling the crack growth and eventually even causes the crack to arrest.

Figure 5A,B illustrates the variation of the SIF and Figure 5C,D the variation of Y_I as a function of crack length for Fix-Fix and Pin-Pin for different L/W ratios. It can be seen from Figure 5A,B that the crack length corresponding to the peak SIF ($[a/W]_{K_{I,\text{Peak}}}$) decreases with decreasing aspect ratio L/W, indicating that crack arrest occurs earlier in a shorter beam.

Figure 6A shows the peak values $[a/W]_{K_{I,\text{Peak}}}$ of Figure 5 versus the beam aspect ratio for the two extreme BC cases Pin-Pin and Fix-Fix. Interestingly, it appears that the relationship between $[a/W]_{K_{I,\text{Peak}}}$ and L/W can be well described by a logarithmic fitting function.

Figure 6B shows the effect of BCs on the FCGR for the SENB geometry under a fatigue loading stress range of $\Delta S_{xx,\text{max}}^{\text{nom}} = 300$ MPa. Similarly to the variations of SIF under various BCs, the FCGR for a crack $a/W \leq 0.1$ is almost the same for all cases, and with the exception of

Rol-Rol, for a longer crack, the FCGR decreases at a specific crack length. It is also seen that pure rotational restraints are less effective compared to horizontal restraints that enable membrane action.

Figure 6C illustrates the FCG histories (a.k.a. a-N curves) for the six key BC cases. In this figure, in order to better compare the crack growth behavior of different cases, the number of cycles is normalized on the basis of the total number of cycles required for a crack to reach a length of $a/W = 0.8$ (named as $N_{0.8}$). A fundamentally different growth behavior is seen in Figure 6C, especially when horizontal displacement is prevented at the supports. It can be inferred that in those cases where the horizontal displacement is restrained in both supports, the crack growth behavior follows a sigmoidal function. In the cases Pin-Pin, Pin-Fix, and Fix-Fix, the crack exhibits accelerated growth, albeit decelerates rapidly soon thereafter when it enters the plateau region of the sigmoidal graph. By adding additional rotational restraints, the crack enters this plateau earlier. Conversely, the behavior follows an exponential function in cases where such restraints are absent, even under rotational restraining.

Figure 7 illustrates the binary tension-compression bending stress (S_{xx}) contours during crack propagation obtained from the FE simulations of the two extreme BC cases Rol-Rol and Fix-Fix. It is seen that for a crack
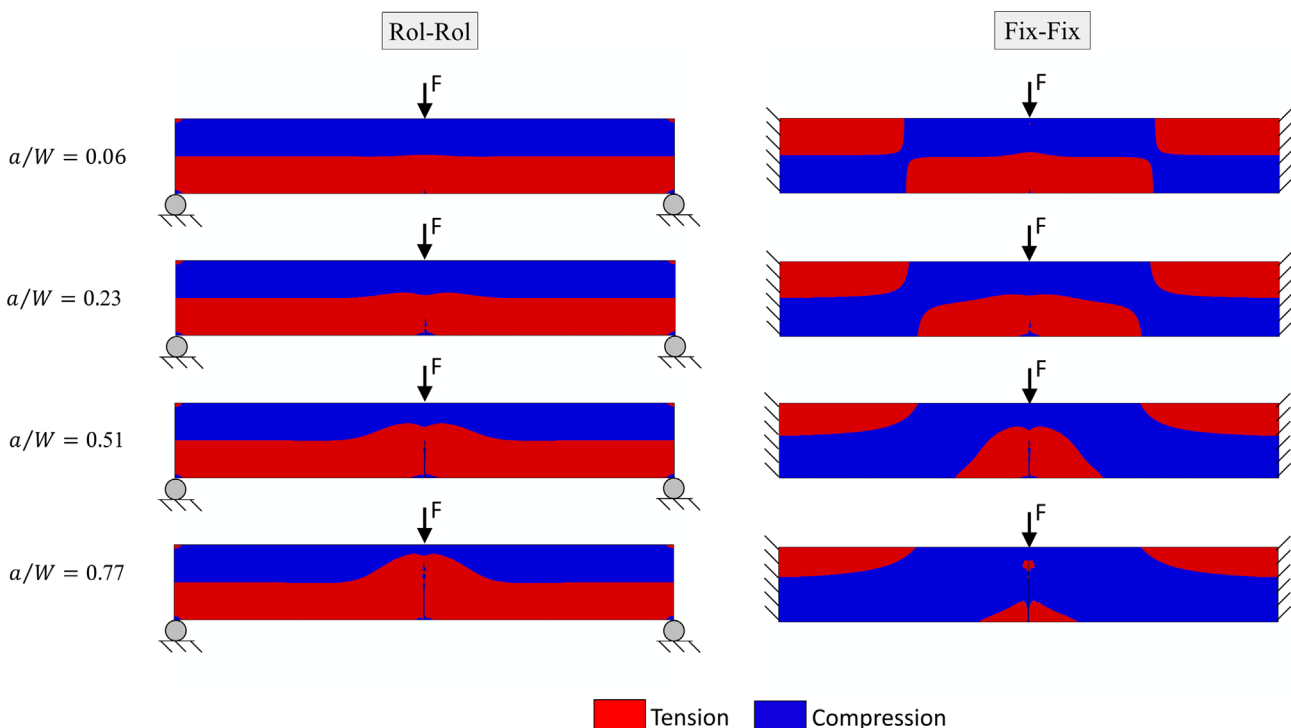

FIGURE 7 Tension-compression bending stress (S_{xx}) contours obtained from the FE crack growth simulation of the two BC cases Rol-Rol and Fix-Fix, for various stages of crack propagation. [Colour figure can be viewed at wileyonlinelibrary.com]

length $a/W \approx 0.06$, the crack in both cases is surrounded by similar tensile stress distributions. In the Rol-Rol case, the primary load-carrying mechanism remains bending, and the crack tip remains at all times located in a pronounced far-field tensile stress region. On the other hand, in the Fix-Fix case, a characteristic redistribution of the tension-compression contours becomes apparent with increasing crack length. At a relative crack depth of $a/W \approx 0.51$, a transition of the global load-carrying mechanism occurs where the far-field compressive stress becomes dominant around the crack tip. To be more precise, a predominant portion of the external load is then carried via a pair of compressive struts forming between the lower end of the supports and the remaining ligament. This membrane action type mechanism leads to a decrease in the crack growth rate, and at a large crack length ($a/W \approx 0.77$), the compressive far-field stress engulfs the entire crack tip, and eventually, a crack arrest occurs.

3.2 | Effect of BCs on the S-N curve

By employing Equation (5), the number of cycles to failure can be predicted, which provides the incentive to generate synthetic S-N curves for all different BC cases. Such generated S-N curves have been plotted in Figure 8

for the SENB geometry with $L/W = 6.67$ for the different BC cases based on a survival probability of 50%. It can be seen that the BC effects presented in Section 3.1 manifest themselves in a change of both the slope and the intercept of the different S-N curves. From this, it can already be inferred that a shift of the "master" S-N curve alone is not sufficient to accommodate the BC effects accurately.

At a shorter fatigue life (or higher applied stress), the difference between the results of various BCs is less pronounced compared to the higher fatigue life (or lower applied stress) since, at a higher stress range, failure occurs at a shorter crack length where the SIF is largely independent of the BCs (c.f. Figure 4). It should be noted that the S-N curve of the Fix-Fix case appears short as the crack arrests at comparatively high stress ranges compared to the Rol-Rol case.

The inverse slope m of all investigated S-N curves is listed in Table 2 for all six BC cases evaluated for different L/W ratios.

A comparison of the values in Table 2 shows that the difference between the inverse slopes of various BCs increases in shorter beams. In other words, the dependency of the inverse slopes on the BCs becomes stronger with decreasing beam aspect ratio. This can be explained by the diminishing compressive strut action with increasing slenderness of the beam.
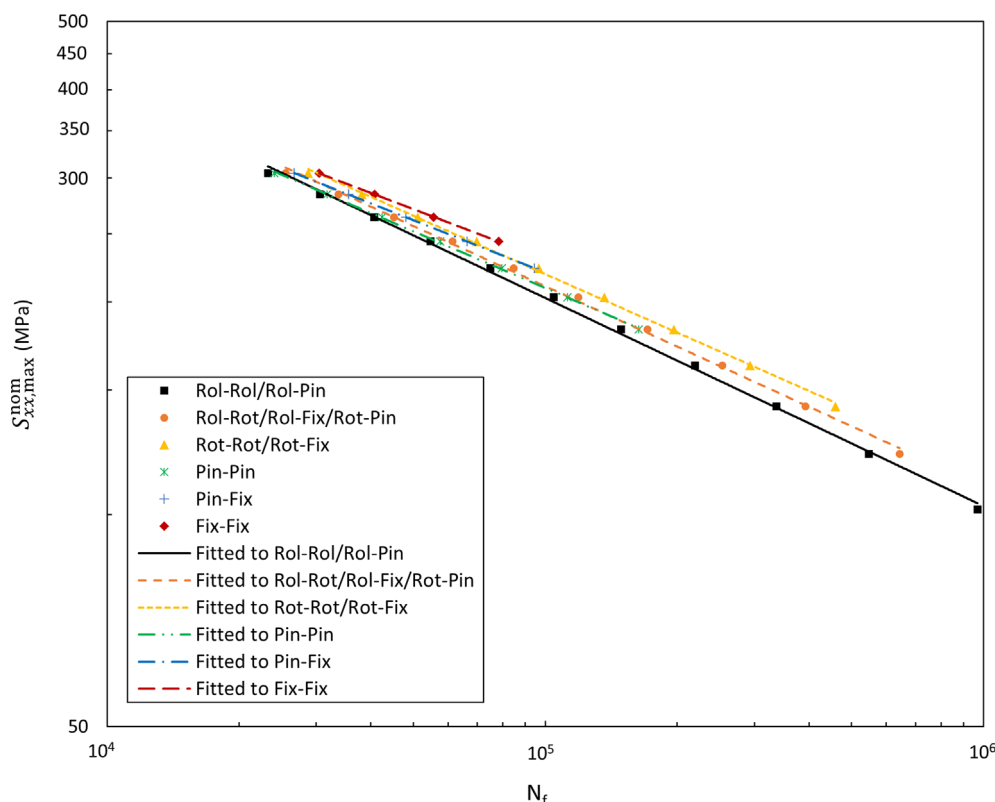

FIGURE 8 Synthetic S-N curves obtained for the SENB geometry with $L/W = 6.67$ for the six different BC cases. Marker points designate the numerical fracture analysis predictions, and the continuous lines represent the fitting power law function. [Colour figure can be viewed at wileyonlinelibrary.com]

4 | PROPOSING A MODEL TO CONSIDER THE EFFECT OF BCS ON S-N CURVES

Figure 8 provides compelling evidence that the BCs indeed significantly influence the fatigue life of otherwise geometrically identical beams subject to the same nominal stress range, which is—at present—not considered in the standards or design codes. In order to take into account the BC effects on the "master" S-N curve, a restraint factor $0 \leq \alpha \leq 1 \in \mathbb{R}$ is proposed. In physical terms, this means that a restraint factor of $\alpha = 0$ corresponds to the unrestrained case (i.e., Rol-Rol BCs), whereas a restraint factor of $\alpha = 1$ corresponds to the fully restrained case (i.e., Fix-Fix BCs). For the intermediate cases (other BCs), α can be determined by assuming that the relation between m and α is linear. The line passing through two points $(m_{\text{Rol-Rol}}, \alpha = 0)$ and $(m_{\text{Fix-Fix}}, \alpha = 1)$ is determined as follows:

$$m = (m_{\text{Fix-Fix}} - m_{\text{Rol-Rol}}) \alpha + m_{\text{Rol-Rol}} \tag{7}$$

Equation (7) provides an equivalent inverse slope reflecting the BC effects through the empirical restraint factor. For each L/W, the values of α for other intermediate BCs were obtained by substituting the values of m presented in Table 2 into Equation (7). Table 3 presents the values of α averaged for various L/W ratios.

Figure 9A shows the values of m normalized with the reference inverse slope of the Rol-Rol case (i.e., unrestrained) denoted as $m_{\text{ref}} = m_{\text{Rol-Rol}}$, as a function of the restraint factor and provided for various L/W ratios. It is apparent that the effect of the BCs on the slope of the S-N curve increases with decreasing beam aspect ratio (L/W). In other words, the influence of the BCs is stronger in shorter beams.

Figure 9A depicts the lines fitted to all data of each L/W ratio. It is seen that the relation between m and α is rather close to a linear relation initially assumed for

TABLE 2 Values of the inverse slope m of S-N curves obtained for the SENB specimen with various aspect ratios (increasing slenderness to the right) separated for the six BC cases.

BCs	L/W				
	3.33	5	6.67	10	13.33
Rol-Rol/Rol-Pin	3.54	3.52	3.49	3.52	3.51
Rol-Rot/Rol-Fix/Rot-Pin	3.95	3.75	3.63	3.59	3.57
Rot-Rot/Rot-Fix	4.10	3.92	3.67	3.64	3.59
Pin-Pin	4.30	3.98	3.79	3.75	3.69
Pin-Fix	4.90	4.38	4.09	3.96	3.82
Fix-Fix	5.47	4.68	4.24	4.05	3.88

TABLE 3 The values of restraint factor for different BCs.

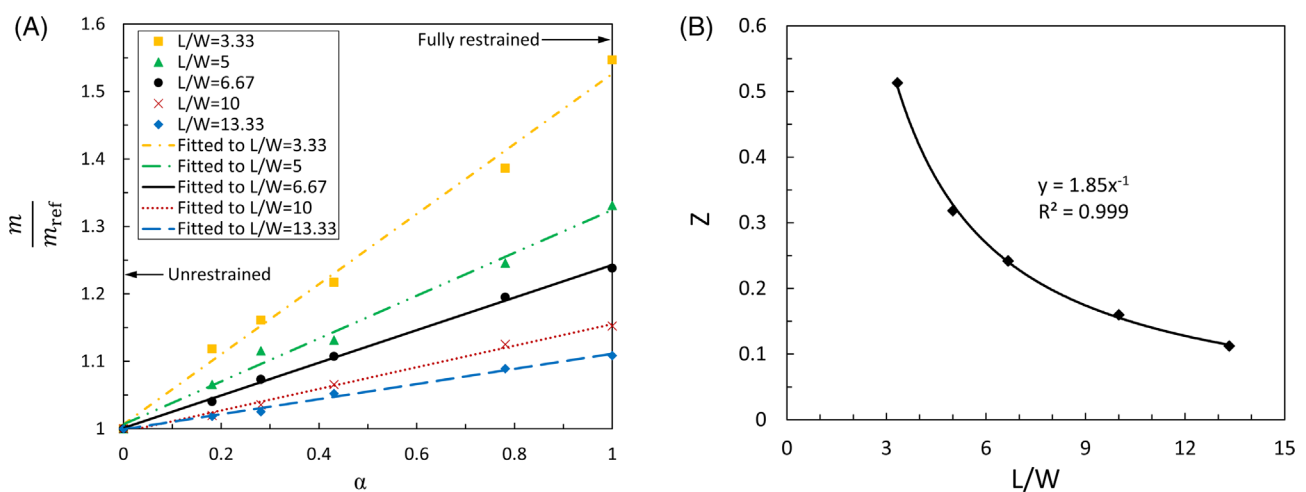| BC	α
Rol-Rol/Rol-Pin	0
Rol-Rot/Rol-Fix/Rot-Pin	0.18
Rot-Rot/Rot-Fix	0.28
Pin-Pin	0.43
Pin-Fix	0.78
Fix-Fix	1

FIGURE 9 (A) Variations of the normalized equivalent inverse slope of the S-N curves as a function of the restraint factor for different L/W ratios. Marker points represent FCG simulations, and continuous lines support the assumption of a linear relation in Equation (8). (B) Variation of Z as a function of the L/W ratio. [Colour figure can be viewed at wileyonlinelibrary.com]

estimating the restraint factor. The linear relation between m and α can be rewritten as follows:

$$\frac{m}{m_{\text{ref}}} = Z\alpha + 1 \qquad (8)$$

In the next step, the variation of the gradient Z with respect to the L/W ratio was investigated, and the results are shown in Figure 9B, where it was found that a hyperbolic function provided a very good fit to the data, that is, $Z \propto 1/x$, which asymptotically approaches the reference slope for slender beams $\lim_{L/W \to \infty} Z\alpha + 1 = 1$ (c.f. Equation 8). Finally, the continuous relation between the inverse slope of the S-N curve and the restraint factor can be expressed for the investigated cases as follows:

$$\frac{m}{m_{\text{ref}}} = 1.85\frac{\alpha}{L/W} + 1 \qquad (9)$$

Repeating the abovementioned procedure for the constant of the S-N curve (A), a relation between this constant and the restraint factor can be achieved as Equation (10):

$$\frac{A}{A_{\text{ref}}} = 1.7\frac{\alpha}{L/W} + 1 \qquad (10)$$

where A_{ref} is the constant of the S-N curve for the Rol-Rol case. Eventually, the modified Basquin law can be obtained by substituting Equations (9) and (10) into Equation (6), leading to the BC-dependent S-N equation, which can be written as follows:

$$N_f = \left(1.7\frac{\alpha}{L/W} + 1\right) A_{\text{ref}} (\Delta S^{\text{nom}})^{\left(1.85\frac{\alpha}{L/W} + 1\right) m_{\text{ref}}} \qquad (11)$$

It should be noted that the proposed approach generates S-N curves for different BCs for a specific geometry. These curves are obtained based on the reference S-N curve, which corresponds to the Rol-Rol BCs for that specific geometry. However, it should be noted that the proposed approach is not limited to a specific geometry. In the following section, the applicability of the model is examined for another geometry.

5 | APPLICATION OF THE PROPOSED MODEL TO THE T-WELDED JOINT

In order to put the proposed modified S-N model to the test, Equation (11) is used to predict the fatigue life of a generic T-welded joint, as depicted in Figure 10A. The predicted fatigue life is subsequently validated through numerical 3D fracture analysis.

The following geometric values were chosen for validation: $L/W = 10$, $H/W = 3.33$, $B/W = 0.33$, $h/W = 0.667$, and $W = 15$ mm. A crack, $a/W = 0.033$, was introduced at the weld toe (c.f. Figure 10A). The mesh was refined around the crack front to ensure the required accuracy. The mesh discretization level was chosen according to a mesh convergence study of the most critical region near the crack front. It was found that a characteristic element size of 0.04 mm in the close vicinity of the crack front provides converged SIF predictions. The model was discretized using 16,390 hexagonal quadratic elements and 79,096 nodes (c.f. Figure 10B). FE simulations were performed for three different cases, namely, Rol-Rol, Pin-Pin, and Fix-Fix.

Figure 11A shows the variation of the SIF as a function of the normalized crack length for the three BC cases. Similarly to the behavior observed in SENB geometry (c.f. Figure 4A), it can be seen in Figure 11A that the difference between the SIFs for the different BCs is small for cracks $a/W \leq 0.3$, while the difference increases for longer cracks $a/W > 0.3$.

Repeating the FCG simulation for several load levels and using the failure criterion $K_{I,\max} = K_{IC}$, number of cycles to failure can be obtained in the same fashion previously performed for the SENB cases.

In order to predict the S-N curves for the T-welded joints using the proposed modified S-N model, the notch stress approach[33] has been employed. The notch stress approach considers the local stress concentration at the notch formed by the weld toe based on the assumption of linear elastic material behavior in the uncracked (intact) model. To take into consideration the weld shape parameters while simultaneously avoiding the stress singularity caused by a sharp corner, a fillet radius of 1 mm was introduced in the weld toe, as illustrated in Figure 10C. The maximum principal hotspot stress at the root of the rounded notch is defined as the notch stress $S_{\text{principal,max}}^{\text{notch}}$. Figure 11B,C shows S-N curves for the two extreme BC cases Pin-Pin and Fix-Fix, based on the notch stress approach.

According to the procedure described in Section 4, the S-N curves for Fix-Fix and Pin-Pin can be predicted by substituting the slope of the reference S-N curve for Rol-Rol and restraint factor α (presented in Table 3) in Equations (9) and (10).

It can be seen in Figure 11B,C that utilization of the reference S-N curve (i.e., Rol-Rol case) for predicting the fatigue life of the BC cases Fix-Fix and Pin-Pin is overly conservative in the high cycle regime. However, the proposed model predicts the S-N curves for

FIGURE 10 (A) Schematic view of the T-welded joint with a symmetric 45° fillet weld showing reference points for BC application, the applied cyclic load and the location of the initial crack; (B) mesh used for the 3D FE simulation in the model with a detailed stress contour plot in the vicinity of the crack; and (C) mesh detail with a fillet radius of 1 mm applied to the weld toe for the notch stress analysis in the model without crack. [Colour figure can be viewed at wileyonlinelibrary.com]
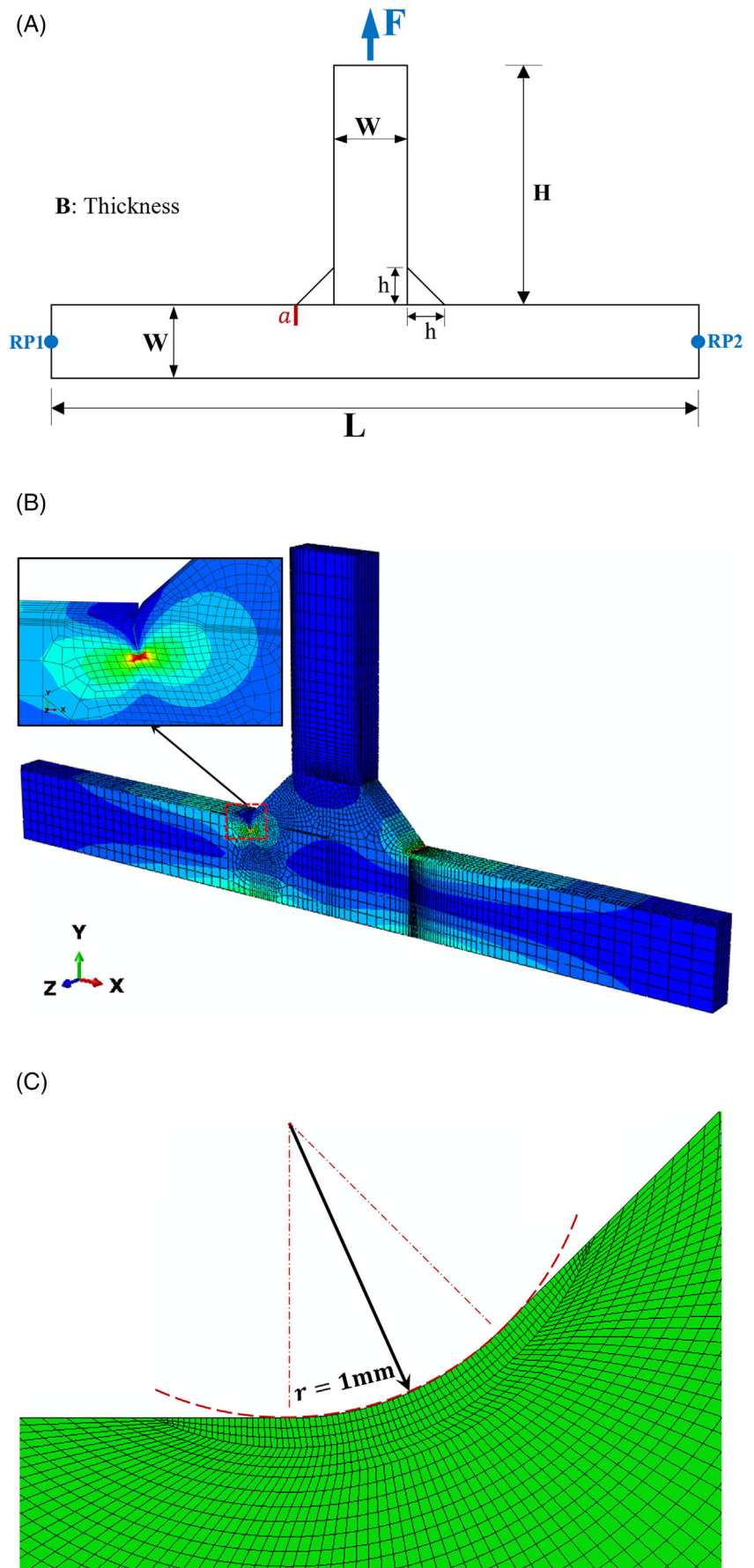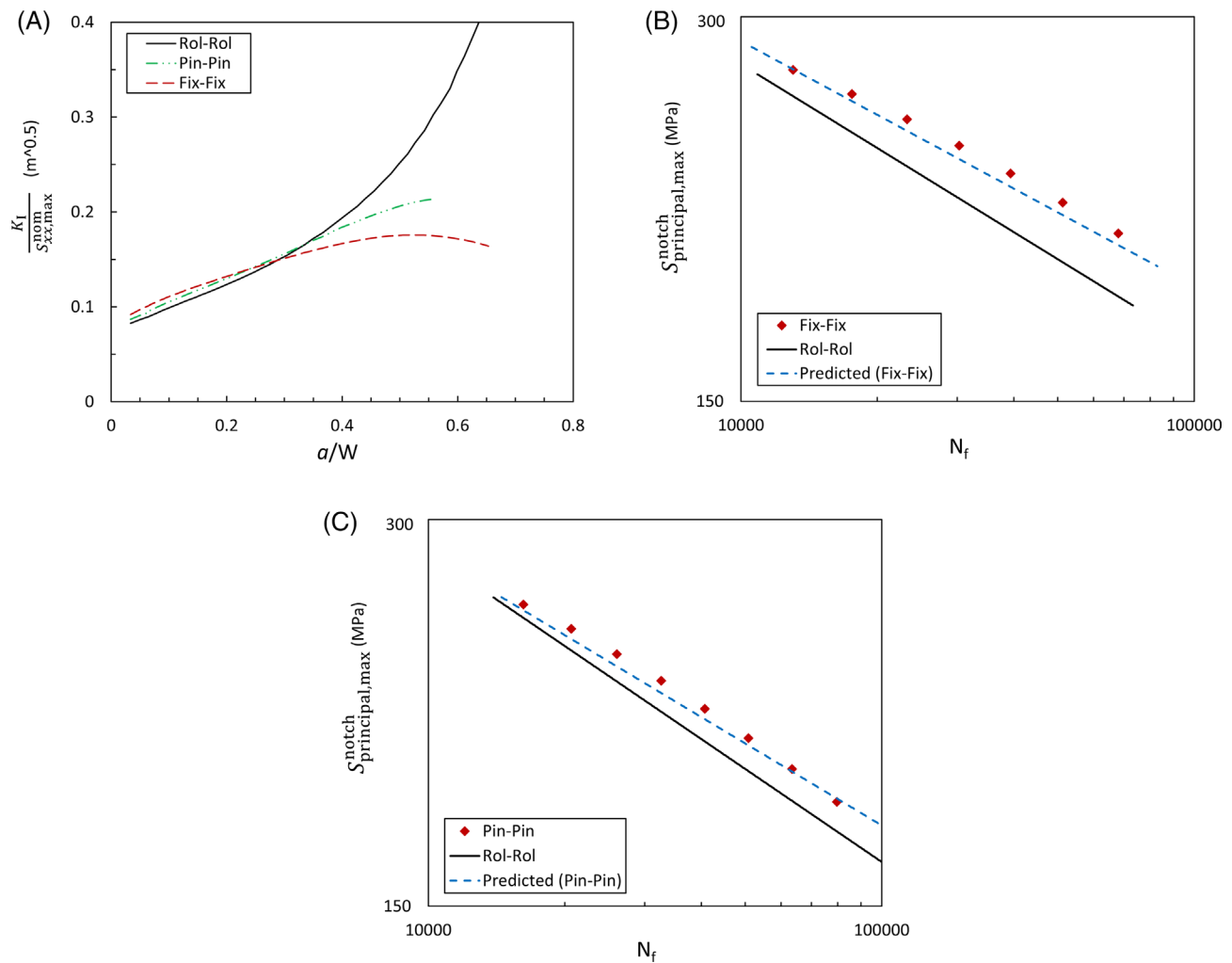
FIGURE 11 (A) Variation of SIF in terms of crack length for different BCs applied to the T-welded joint. Benchmark validation of the predicted S-N curves based on the proposed model versus 3D numerical fracture analysis (diamond markers) on the example of a T-welded joint for the two BC cases: (B) Fix-Fix and (C) Pin-Pin. [Colour figure can be viewed at wileyonlinelibrary.com]

various BCs with significantly improved accuracy, as corroborated by the good agreement with the 3D FEA predictions. It is noteworthy to mention that the impact of the proposed model gains significance with increasing cycle numbers.

The proposed model is used as an example to demonstrate the possibility to modify SN-curves to account for the effect of BCs. In this example, the geometry of the weld toe was idealized, and it is assumed that there are no residual stresses. Also, it should be noted that the same initial crack size is assumed for generating S-N data across various BCs. However, in practical scenarios, the initial crack size may vary among different specimens due to welding defects. Further investigations and experimental data are needed to generalize the approach for other types of welded joints.

6 | EXPERIMENTAL INVESTIGATION OF THE EFFECT OF BCS ON FCGR

To validate the observed trend of FCG in the FE simulations, an experimental setup was prepared to examine the influence of two extreme BCs, namely, the Rol-Rol and Fix-Fix case.

A hot-rolled sheet of structural steel S235 with a thickness of 15 mm was utilized in the present investigation. As shown in Figure 12, 4-point bending FCG tests were conducted on the SENB specimen for both, the Rol-Rol and the Fix-Fix case. For each case, one specimen was tested. Figure 12B depicts the test setup specifically designed for the Fix-Fix case in this study, which involved the use of a series of bolts to restrict rotation as
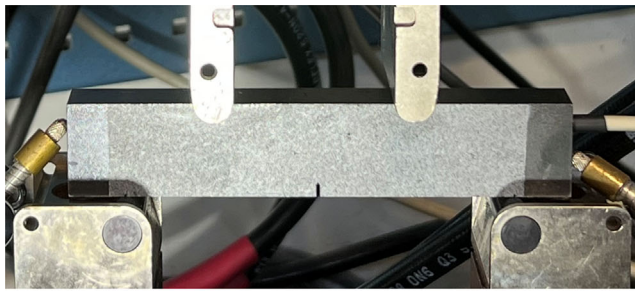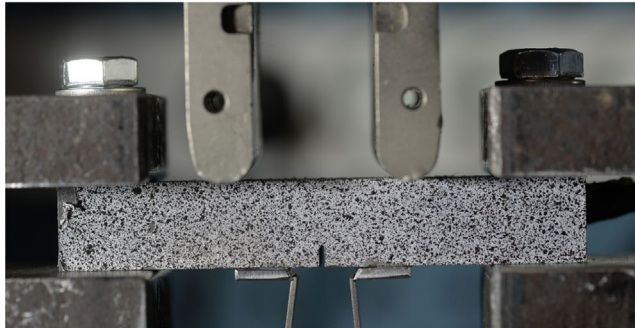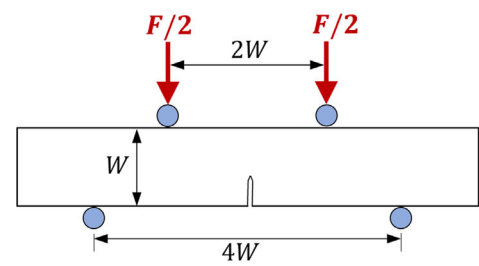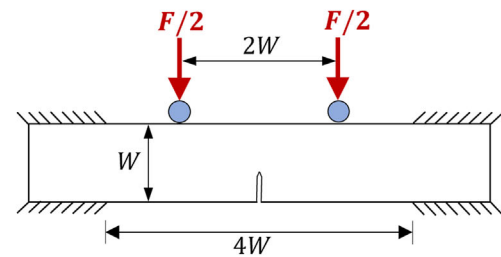
FIGURE 12 4-point bending FCG test set-up with specimen for (A) Rol-Rol BCs and (B) Fix-Fix BCs. [Colour figure can be viewed at wileyonlinelibrary.com]

well as horizontal and vertical displacements of the specimen ends in the clamped region. The widths of the specimens W are 25 and 15 mm for the Rol-Rol and Fix-Fix cases, respectively. The initial notch was created through electro-discharge machining. Fatigue precracking was performed until the initial crack length reached 4 mm for both cases.

The experiments were conducted using an MTS 25 kN servo-hydraulic fatigue machine. The loads were applied sinusoidally at a frequency of 5 Hz, and a constant loading ratio (R) of 0.1 was maintained. The maximum applied loads were 16.7 kN for the Rol-Rol case and 18.0 kN for the Fix-Fix case. Crack gauges were adhered in front of the notch to measure the crack length. As the crack propagated, the grid lines, which were aligned at intervals of 0.1 mm, became disconnected one after another, resulting in a change in output value through an adaptor. In the case of Fix-Fix BCs, due to the very low propagation rate and displacement, a clip gauge was additionally employed to measure the crack length.

Figure 13A depicts the results of FCGR for Rol-Rol and Fix-Fix BCs. Consistent with the findings from the

FE simulations, the FCGR for the Fix-Fix BCs initially increases for a crack $a/W < 0.4$, and for a longer crack ($a/W > 0.4$), the FCGR decreases insofar as the crack arrest occurs after 3×10^6 cycles.

FE simulations of FCG in the current SENB specimens under BCs illustrated in Figure 12 were performed as described in Section 2.2. The results of the experiments and FE analysis are presented in Figure 13B,C. It can be observed in Figure 13C that the trend of crack propagation aligns with the findings from the FE analysis (Figure 6C). Unlike the Rol-Rol BCs, the FCGR in the case of Fix-Fix BCs decreases after $a/W = 0.75$. The experimental results for Fix-Fix BCs indicate that the crack growth rate decreases to almost zero (i.e., crack arrest) when the crack length reaches $a/W = 0.75$, which closely matches the FEA prediction of $a/W = 0.74$. Overall, there is good agreement between the predicted and experimental results for both BCs. However, a slight disparity can be observed between the predicted and experimental results for Fix-Fix BCs at a crack length of $a/W \geq 0.6$, which may be attributed to a small slip occurring between the clamps and the specimen during crack propagation.
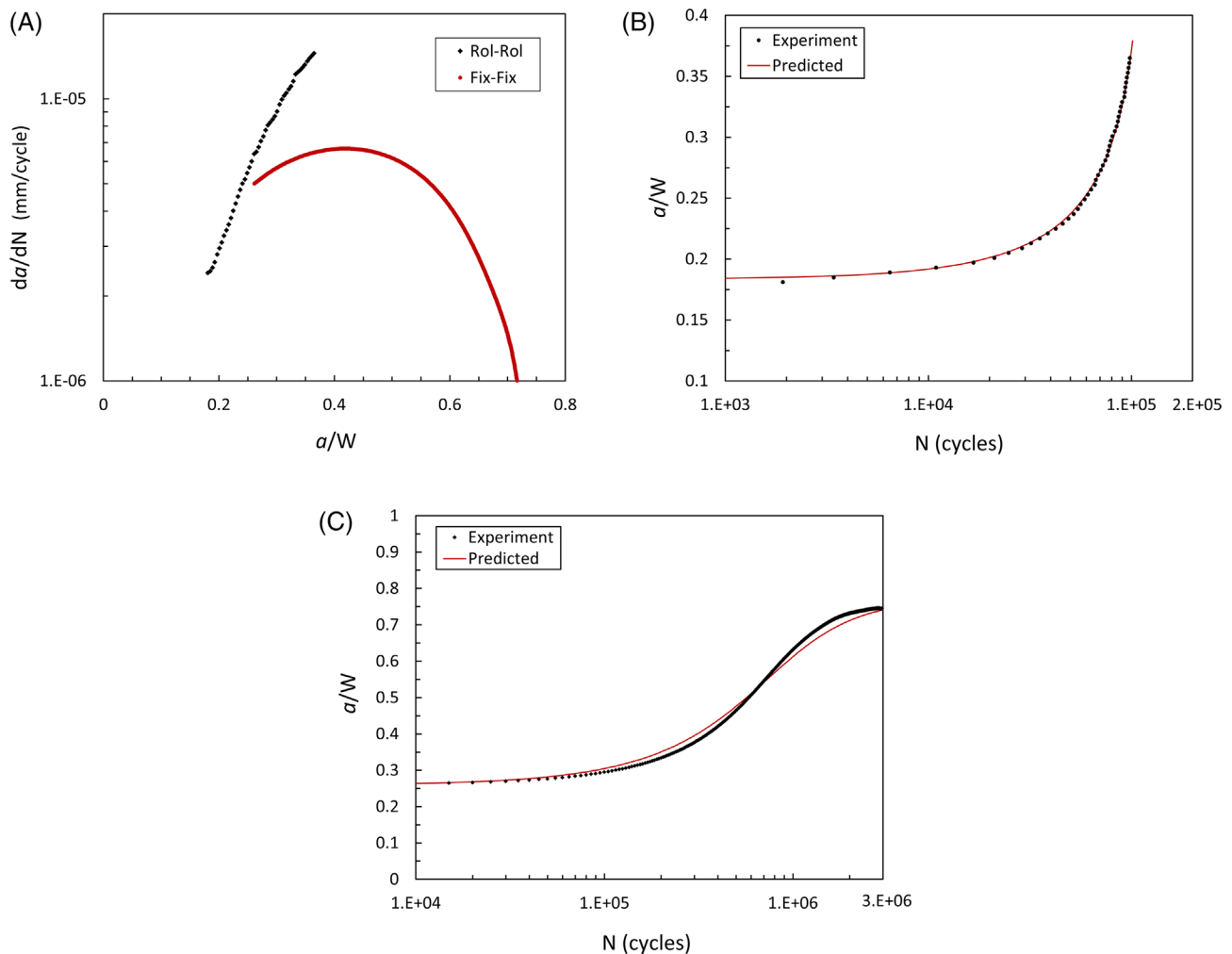
FIGURE 13 (A) Results of FCGR for Rol-Rol and Fix-Fix BCs. Experimentally obtained and numerically predicted results of FCG for (B) Rol-Rol BCs and (C) Fix-Fix BCs. [Colour figure can be viewed at wileyonlinelibrary.com]

7 | CONCLUSIONS

Based on the numerical fracture mechanics analysis, a modified S-N model is proposed with the capability to accurately consider the effect of different BCs on the crack propagation as well as fatigue life of components with identical geometry and subject to the same nominal stress range. The following key findings can be drawn from this investigation:

- The SIF of a crack $a/W \leq 0.1$ is largely independent of the prevailing BCs, while the latter has an increasing effect on the SIF for cracks $a/W > 0.2$. Contrary to the simply supported BC, the SIF initially increases and then decreases at a specific crack length, and a crack growth retardation occurs. In such cases, the crack growth behavior no longer follows an exponential function but rather follows a sigmoidal-type function.

- It was observed that for a crack $0.2 < a/W < 0.5$, restraining the rotation of the beam has a greater influence on controlling the crack growth, while for a larger crack ($a/W > 0.5$), restraining the horizontal displacement has a more pronounced effect on controlling crack growth.

- A crack arrest ($K_I \rightarrow 0$) can be achieved by restraining the horizontal displacements, which in the investigated cases entailed a predominant compressive stress field around the crack tip.

- It was seen that the BCs affect the slope of the S-N curve, which consequently has a substantial impact on fatigue life. This effect is more significant at lower applied stress ranges. It was also observed that as the length of the beam becomes shorter, the influence of the BCs on the slope of the S-N curve becomes greater.

- It was shown that the proposed model could predict the S-N curves for a T-welded joint specimen subjected to various BCs well.

- The experimental results demonstrated that the restriction of specimen end displacements has a significant effect on the FCGR, ultimately resulting in crack arrest.

NOMENCLATURE

A	constant of S-N curve
A_{ref}	constant of S-N curve for simply supported case
a	crack length
a_c	critical crack length
a_i	initial crack length
B	thickness of specimen
C_p	material parameter in Paris equation
E	Young's modulus
F	applied force
I	second-area moment
J_{int}	interaction integral
K_I	stress intensity factor of mode I
K_{IC}	fracture toughness
K_{II}	stress intensity factor of mode II
L	length of specimen
M	bending moment
M_S	reaction bending moment
m	inverse slope of S-N curve
m_{ref}	inverse slope of S-N curve for simply supported case
N	number of cycles
N_f	number of cycles to failure
N_S	horizontal reaction force
n_p	material parameter in the Paris equation
R	loading ratio
R_S	vertical reaction force
$S_{xx,max}^{nom}$	maximum nominal stress in X direction
$S_{principal,max}^{notch}$	maximum principal stress
W	width of specimen
Y_I	dimensionless stress intensity factor of mode I
α	restraint factor
ν	Poisson's ratio

DATA AVAILABILITY STATEMENT

The data that support the findings of this study are available from the corresponding author upon reasonable request.

ORCID

Iman Shakeri https://orcid.org/0000-0001-6833-6609

REFERENCES

1. Lotsberg I. *Fatigue Design of Marine Structures.* Cambridge University Press; 2016.
2. EN 1993-1-9. *Eurocode 3: Design of Steel Structures - Part 1-9: Fatigue* 2005.
3. Hobbacher AF. *Recommendations for Fatigue Design of Welded Joints and Components.* 2nd ed. IIW Collection; 2016.
4. DNV-RP-C203. *Fatigue Design of Offshore Steel Structures.* DNV; 2019.
5. Etube L. *Fatigue and Fracture Mechanics of Offshore Structures.* US; 2001.
6. Pucillo GP, Espositob L, Leonetti D. On the effects of unilateral boundary conditions on the crack growth rate under cycling bending loads. *Int J Fatigue.* 2019;124:245-252.
7. Zerbst U, Lundén R, Edel KO, Smith RA. Introduction to the damage tolerance behaviour of railway rails—a review. *Eng Fract Mech.* 2009;76(17):2563-2601.
8. Sun D, Gan J, Wang Z, Luo P, Wu W. Experimental and analytical investigation of fatigue crack propagation of T-welded joints considering the effect of boundary condition. *Fatigue Fract Eng Mater Struct.* 2017;40(6):894-908.
9. Pucillo GP, Espositob L, Leonetti D. Boundary conditions effects on the crack growth mechanism under cycling bending. In: *Utah: 2019 ASME Joint Rail Conference*; 2019.
10. Mlikota M, Schmauder S, Božić Ž. Calculation of the Wöhler (S-N) curve using a two-scale mode. *Int J Fatigue.* 2018;114:289-297.
11. Mlikota M, Dogahe K, Schmauder S, Božić Ž. Influence of the grain size on the fatigue initiation life curve. *Int J Fatigue.* 2022;158:106562.
12. Mlikota M, Schmauder S, Božić Ž, Hummel M. Modelling of overload effects on fatigue crack initiation in case of carbon steel. *Fatigue Fract Eng Mater Struct.* 2017;40(8):1182-1190.
13. Shakeri I, Shahani AR, Rans CD. Fatigue crack growth of butt welded joints subjected to mixed mode loading and overloading. *Eng Fract Mech.* 2021;241:107376.
14. Barsoum Z, Barsoum I. Residual stress effects on fatigue life of welded structures using LEFM. *Eng Fail Anal.* 2009;16(1):449-467.
15. Božić Ž, Schmauder S, Mlikota M, Hummel M. Multiscale fatigue crack growth modelling for welded stiffened panels. *Fatigue Fract Eng Mater Struct.* 2014;37(9):1043-1054.
16. Božić Ž, Schmauder S, Wolf H. The effect of residual stresses on fatigue crack propagation in welded stiffened panels. *Eng Fail Anal.* 2018;84:346-357.
17. Tang L, Ince A, Zheng J. Numerical modeling of residual stresses and fatigue damage assessment of ultrasonic impact treated 304L stainless steel welded joints. *Eng Fail Anal.* 2020;108:104277.
18. Ince A. Computational crack propagation modeling of welded structures under as-welded and ultrasonic impact treatment conditions. *Fatigue Fract Eng Mater Struct.* 2022;45(2):578-592.
19. Shahani AR, Shakeri I. Experimental evaluation of fatigue behavior of thin Al5456 welded joints. *Fatigue Fract Eng Mater Struct.* 2020;43(5):965-977.
20. Zerres P, Vormwald M. Review of fatigue crack growth under non-proportional mixed-mode loading. *Int J Fatigue.* 2014;58:75-83.

21. Petinov SV, Reemsnyder HS, Thayamballi AK. The similitude of fatigue damage principle: application in S-N curves-based fatigue design. In: Marquis G, Solin S, eds. *Fatigue Design and Reliability*. European Structural Integrity Society; 1999: 219-228.

22. Shahani AR, Shakeri I. Analysis of a functionally graded finite wedge under antiplane deformation. *J Solid Mech*. 2022;14: 291-311.

23. Shahani AR, Shakeri I, Rans CD. Effect of residual stress redistribution and weld reinforcement geometry on fatigue crack growth of butt welded joints. *Int J Fatigue*. 2020;139: 105780.

24. Singh VK, Gope PC, Bhagat RK. Effect of boundary condition on pre-existing crack under fatigue loading. *J Solid Mech*. 2011; 3:198-207.

25. Systèmes D. *Abaqus Product Documentation: Abaqus Analysis User's Manual. Version 2021*. US; 2021.

26. Zentech International Limited. *Zencrack User Manual*. Version 8.3–1. Zentech International Limited; 2018.

27. Shahani AR, Shakeri I, Rans CD. Fatigue crack growth of Al 5083–H111 subjected to mixed–mode loading. *J Braz Soc Mech Sci Eng*. 2020;42(8):442.

28. *Python*. Version 3.10. 2021. Available from: https://www.python.org/

29. He Z, Kotousov A, Berto F, Branco R. A brief review of recent three-dimensional studies of brittle fracture. *Phys Mesomech*. 2016;19(1):6-20.

30. Xin H, Veljkovic M. Residual stress effects on fatigue crack growth rate of mild steel S355 exposed to air and seawater environments. *Mater des*. 2020;193:108732.

31. Shakeri I, Danielsen HK, Tribhou A, Fæster S, Mishin OV, Eder MA. Effect of manufacturing defects on fatigue life of high strength steel bolts for wind turbines. *Eng Fail Anal*. 2022;141:106630.

32. Fett T. *Stress Intensity Factors - T-Stresses - Weight Functions*. University of Karlsruhe; 2008.

33. Fricke W. *IIW Recommendations for the Fatigue Assessment of Welded Structures by Notch Stress Analysis*. Woodhead Publishing; 2012.